nanomaterials

MDPI

Article

Composite Magnetic Photocatalyst $Bi_5O_7I/Mn_xZn_{1-x}Fe_2O_4$: Hydrothermal-Roasting Preparation and Excellent Photocatalytic Activity

Hailong Wang [1], Longjun Xu [1,*], Chenglun Liu [1,2], Yuan Lu [1], Qi Feng [1], Tingzeng Wu [1] and Ruiqi Wang [1]

[1] State Key Laboratory of Coal Mine Disaster Dynamics and Control, Chongqing University, Chongqing 400044, China; cqyywhl@163.com (H.W.); xlclj@cqu.edu.cn (C.L.); cquluyuan@126.com (Y.L.); 18223208007@163.com (Q.F.); tingzengyeh@163.com (T.W.); HYQWRO1314@163.com (R.W.)

[2] College of Chemistry and Chemical Engineering, Chongqing University, Chongqing 400044, China

* Correspondence: xulj@cqu.edu.cn; Tel.: +86-137-5282-0583

Received: 17 December 2018; Accepted: 15 January 2019; Published: 18 January 2019

Abstract: A new composite magnetic photocatalyst, $Bi_5O_7I/Mn_xZn_{1-x}Fe_2O_4$, prepared by a hydrothermal-roasting method was studied. The photocatalytic properties of $Bi_5O_7I/Mn_xZn_{1-x}Fe_2O_4$ were evaluated by degradation of Rhodamine B (RhB) under simulated sunlight irradiation, and the structures and properties were characterized by X-ray diffraction (XRD), Fourier-transform infrared spectroscopy (FTIR), scanning electron microscopy (SEM), transmission electron microscopy (TEM), ultraviolet-visible light (UV-Vis) diffuse reflectance spectra (DRS), and a vibrating sample magnetometer (VSM). The results indicated that $Bi_5O_7I/Mn_xZn_{1-x}Fe_2O_4$ was an orthorhombic crystal, which was similar to that observed for Bi_5O_7I. $Bi_5O_7I/Mn_xZn_{1-x}Fe_2O_4$ consisted of irregularly shaped nanosheets that were 40–60 nm thick. The most probable pore size was 24.1 nm and the specific surface area was 7.07 m^2/g. $Bi_5O_7I/Mn_xZn_{1-x}Fe_2O_4$ could absorb both ultraviolet and visible light, and the energy gap value was 3.22 eV. The saturation magnetization, coercivity and residual magnetization of $Bi_5O_7I/Mn_xZn_{1-x}Fe_2O_4$ were 3.9 emu/g, 126.6 Oe, and 0.7 emu/g respectively, which could help $Bi_5O_7I/Mn_xZn_{1-x}Fe_2O_4$ be separated and recycled from wastewater under the action of an external magnetic field. The recycling experiments revealed that the average recovery rate of the photocatalyst was 90.1%, and the photocatalytic activity was still more than 81.1% after five cycles.

Keywords: magnetic photocatalyst; $Bi_5O_7I/Mn_xZn_{1-x}Fe_2O_4$; hydrothermal-roasting method

1. Introduction

In recent years, with the progress of nanotechnology and the application of photocatalytic technology in environmental pollution treatment [1–3], lots of semiconducting metal-oxide nanostructures were widely used for water purification due to their great photocatalytic performance [4,5]. Grottrup [6] applied Bi for doping ZnO, which significantly enhanced its ability in the photocatalytic degradation of methylene blue. Huang [7] indicated that the rate constant of degradation of 17 β-estradiol over N-doped Bi_2O_3 was 6.3 times that obtained over Bi_2O_3. Oppong [8] pointed out that the reason for the better photocatalytic performance of Gd–TiO_2–graphene oxide (GO) nanocomposites compared to pure TiO_2 was because GO sheets and Gd^{3+} ions are excellent co-catalysts and their presence promotes the reaction sites. Currently, bismuth-based nanometer semiconductors are one of the research hotspots in the field of photocatalytic materials due to their unique electronic structure and excellent absorption ability of ultraviolet and visible light [9–12]. Bi_5O_7I, an oxygen-rich bismuth-based

nanometer semiconductor [13–15], is composed of a Bi 6*p* orbital at the bottom of the conduction band and Bi 6*s*, O 2*p*, and I 5*p* orbitals at the top of the valence band [16,17]. The Bi 6*s* and O 2*p* orbitals can form several dispersed hybrid valence bands, while the I 5*p* orbital disperses the valence bands further [18,19]. Consequently, the above results accelerate the migration of photo-generated holes and promote the occurrence of oxidation reactions [20,21]. Sun et al. thought that the Bi_5O_7 and I sections form a unique hierarchical structure successively along the c-axis orderly. As an accelerator for the separation of photo-generated electron–hole pairs, the permanent electrostatic field between the layers can improve the photocatalytic activity of Bi_5O_7I [22]. Xia et al. prepared sheets of Bi_5O_7I using the calcining method. However, the photocatalytic degradation rate of Bi_5O_7I (0.1 g) for Rhodamine B (RhB) solution (100 mL, 10mg/L) was only 52% in 120 min under simulated sunlight irradiation [23]. In order to enhance the photocatalytic activity of Bi_5O_7I, some means were mentioned, such as doping and compounding [24–27]. The photocatalytic degradation rate of Eu (3%)/Bi_5O_7I microspheres was 2.8 times that of Bi_5O_7I [28], and the photocatalytic degradation efficiency of a graphitic carbon nitride (g-C_3N_4) (10%)–Bi_5O_7I nanocomposite was 1.4 times that of Bi_5O_7I [29].

Most organic pollutants in wastewater can be degraded using photocatalytic technology, with good degradation effects and no secondary pollution. Nevertheless, the complex process, large energy consumption, and low recovery rate are the main disadvantages of the common recovery method, because photocatalytic materials disperse in wastewater uniformly [30]. $Mn_xZn_{1-x}Fe_2O_4$ is a soft magnetic ferrite material with its own benefits, such as high saturation magnetization, high permeability, low coercive force, low loss, strong stability, and so on [31]. Therefore, composite magnetic photocatalytic materials prepared with $Mn_xZn_{1-x}Fe_2O_4$ as a magnetic matrix can achieve the goal of magnetic recovery, and the heterojunction formed between $Mn_xZn_{1-x}Fe_2O_4$ and the photocatalyst is conducive to enhancing the photocatalytic activity of the composite. For instance, Zhang et al. [32] synthesized a $Mn_xZn_{1-x}Fe_2O_4$/α-Bi_2O_3 composite magnetic photocatalyst using the dip-calcination method. However, the recovery rate was only 84.1% under the action of an external magnet, and the degradation time was more than four hours when the degradation rate attained 86.2% after five recoveries. The energy consumption of the preparation process is tremendous, because the precursor of $Mn_xZn_{1-x}Fe_2O_4$ must be calcined at 1200 °C for three hours. In addition, the synthesis of composite magnetic photocatalytic materials using Bi_5O_7I as a photocatalyst and $Mn_xZn_{1-x}Fe_2O_4$ as the magnetic matrix is rarely reported.

To overcome these shortcomings, a $Bi_5O_7I/Mn_xZn_{1-x}Fe_2O_4$ composite magnetic photocatalyst was prepared using a hydrothermal-roasting method, and the structures and properties were characterized by X-ray diffraction (XRD), Fourier-transform infrared spectroscopy (FTIR), scanning electron microscopy (SEM), transmission electron microscopy (TEM), ultraviolet-visible light (UV-Vis) diffuse reflectance spectra (DRS), and a vibrating sample magnetometer (VSM). In the meantime, the activity and stability of $Bi_5O_7I/Mn_xZn_{1-x}Fe_2O_4$ were evaluated through the degradation of RhB under simulated sunlight irradiation.

2. Materials and Methods

Analytical reagents of $Bi(NO_3)_3{\cdot}5H_2O$, KI, $C_2H_6O_2$, $Fe_2(SO_4)_3$, $MnSO_4{\cdot}H_2O$, $ZnSO_4{\cdot}7H_2O$, NaOH, $C_{28}H_{31}ClN_2O_3$, and HNO_3 were used as raw materials for sample preparation, and were provided by Chengdu Kelong Chemical Ltd (Chengdu, China).

2.1. Preparation of $Bi_5O_7I/Mn_xZn_{1-x}Fe_2O_4$

$Mn_xZn_{1-x}Fe_2O_4$ was prepared using a hydrothermal method. Firstly, according to the molar ratio of n(MnO):n(ZnO):n(Fe_2O_3) = 3.28:1.33:5.39, $ZnSO_4{\cdot}7H_2O$, $MnSO_4{\cdot}H_2O$, and $Fe_2(SO_4)_3$ were dissolved in deionized water. Then, 5 M NaOH aqueous solution was added dropwise to adjust the pH value of the solution to 13 under vigorous stirring. Subsequently, the solution was transferred into a Teflon-lined autoclave for reaction at 200 °C for 5 h. Afterward, the resulting precipitates were

washed with deionized water, as well as dilute sulfuric acid, several times, before being dried at 80 °C for 12 h.

$Bi_5O_7I/Mn_xZn_{1-x}Fe_2O_4$ was prepared using a hydrothermal-roasting method. Firstly, 5 mL of ethylene glycol (EG) was dissolved in 35 mL of deionized water with stirring for 10 min to gain solution A. Then, 2 mmol Bi $(NO_3)_3 \cdot 5H_2O$ and 2 mmol KI were continuously dissolved in solution A while stirring to acquire suspension liquid B. Then, 10 wt.% as-prepared $Mn_xZn_{1-x}Fe_2O_4$ was added into suspension liquid B with continuous stirring for 60 min. Afterward, the mixed turbid solution was transferred into a Teflon-lined autoclave for reaction at 160 °C for 12 h, and the resulting precipitates were washed with deionized water several times. Finally, the precipitates were dried at 80 °C for 5 h and roasted at 480 °C for 2 h in a muffle, obtaining $Bi_5O_7I/Mn_xZn_{1-x}Fe_2O_4$. The synthetic process is displayed in Scheme 1.

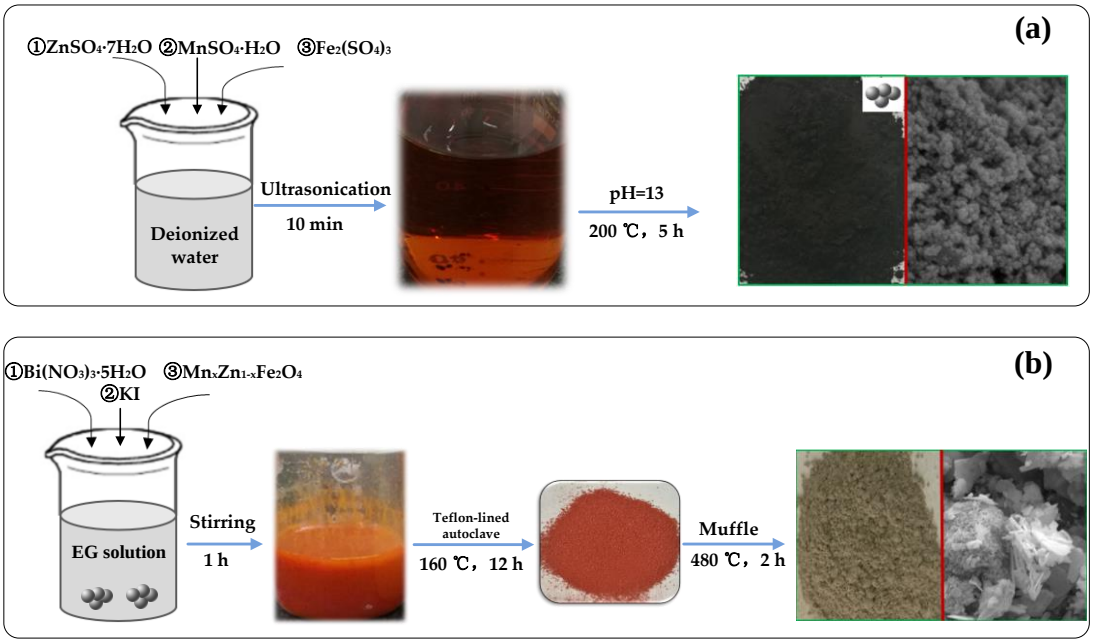

Scheme 1. Schematic illustration of the synthetic process for (**a**) $Mn_xZn_{1-x}Fe_2O_4$ and (**b**) $Bi_5O_7I/Mn_xZn_{1-x}Fe_2O_4$.

2.2. Characterization

The structures of the as-prepared products were characterized by X-ray diffraction (XRD; Shimadzu, XRD-6000, Shimadzu, Kyoto, Japan) and Fourier-transform infrared spectroscopy (FTIR; Nicolet iS50, Thermo Fisher Scientific, Waltham, MA, USA). The morphologies and microstructures of the products were observed using scanning electron microscopy (SEM; S4800, Hitachi, Tokyo, Japan) and transmission electron microscopy (TEM; Tecnai G2F20, FEI, Hillsboro, OR, USA). The surfaces and apertures of the products were measured using an automatic multistation surface and aperture analyzer (Quadrasorb 2MP, Quantachrome, Boynton Beach, FL, USA). The element contents in the composite were analyzed by X-ray photoelectron spectroscopy (XPS, ESCALAB250Xi, Thermo Fisher Scientific, Waltham, MA, USA). The optical absorption ability and magnetic performance of the products were identified with UV-Vis diffuse reflectance spectra (UV-Vis DRS; TU1901, Beijing, China) and a vibrating sample magnetometer (VSM; 7410, Lake Shore, Westerville, OH, USA) respectively.

2.3. Photocatalytic Evaluation

The photocatalytic properties of the samples were evaluated through the degradation of Rhodamine B (RhB) under simulated sunlight irradiation. Firstly, 0.1 g of photocatalyst and 100 mL of RhB aqueous solution (10 $mg \cdot L^{-1}$) were put into a beaker and stirred for 30 min in the dark to reach the adsorption

balance. Then, the mixtures were irradiated with a xenon lamp (CEL-HXF3000, AULTT) of 300 W, and the ultraviolet-visible emission spectrum. Then, 4 mL of the solution was withdrawn at set time intervals, before being centrifuged at 4000 rpm for 5 min to get the supernatant. Finally, the characteristic absorbance of RhB was measured using a UV-Vis spectrophotometer.

3. Results and Discussion

3.1. Structure Characteristics

Figure 1 presents the XRD patterns of $Mn_xZn_{1-x}Fe_2O_4$, Bi_5O_7I, and $Bi_5O_7I/Mn_xZn_{1-x}Fe_2O_4$. As displayed, the diffraction peaks, located at 28.24°, 31.23°, 33.14°, 33.55°, 47.82°, 53.60°, and 56.12°, were assigned to the (312), (004), (204), (020), (224), (316), and (912) planes of orthorhombic Bi_5O_7I (JCPDS file No. 40-0538). Neither the preferred growth direction nor the crystal structure of Bi_5O_7I were changed by $Mn_xZn_{1-x}Fe_2O_4$, because the characteristic peaks of $Bi_5O_7I/Mn_xZn_{1-x}Fe_2O_4$ were basically consistent with Bi_5O_7I. Interestingly, the peak of the (912) plane of $Bi_5O_7I/Mn_xZn_{1-x}Fe_2O_4$ overlapped with the (511) plane of the $Mn_xZn_{1-x}Fe_2O_4$. The average crystalline size of $Bi_5O_7I/Mn_xZn_{1-x}Fe_2O_4$ was 71.3 nm, as calculated using the Scherrer formula. The cell parameters were as follows: a = 16.8036 Å, b = 5.0721 Å, c = 11.7316 Å, $\alpha = \beta = \gamma = 90°$.

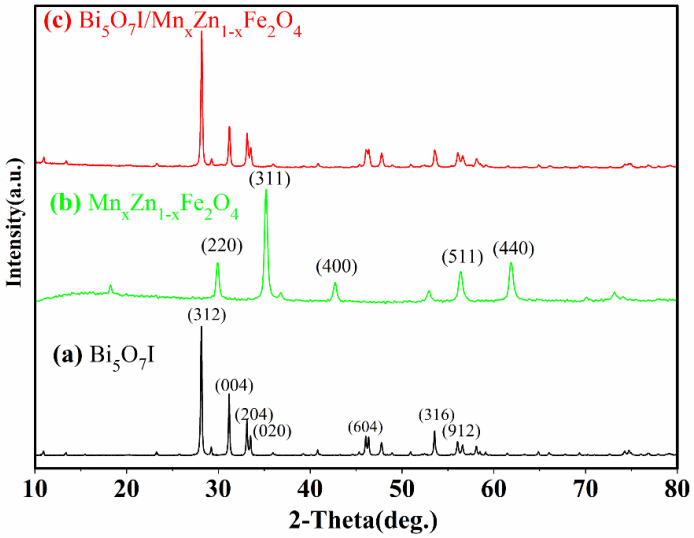

Figure 1. (**a**) X-ray diffraction (XRD) patterns of Bi_5O_7I; (**b**) XRD patterns of $Mn_xZn_{1-x}Fe_2O_4$; (**c**) XRD patterns of $Bi_5O_7I/Mn_xZn_{1-x}Fe_2O_4$.

The FTIR spectra of $Mn_xZn_{1-x}Fe_2O_4$, Bi_5O_7I, and $Bi_5O_7I/Mn_xZn_{1-x}Fe_2O_4$ are shown in Figure 2. The characteristic peaks at 3434 cm^{-1} and 2360 cm^{-1} were attributed to the stretching vibration and bending vibration of the hydroxyl group (–OH) from surface-adsorbed water, respectively [33]. Typical Raman bands of the Fe–O–Fe bond and the stretching vibration of the Zn–O bond were located at 1399 cm^{-1} and 568 cm^{-1}, respectively [34]. The intensive signals around 1389 cm^{-1}, 846 cm^{-1}, and 610 cm^{-1} referred to the bending vibration of the Bi–O bond, and 491 cm^{-1} referred to the stretching vibration of the Bi–O bond [35]. Figure 2c indicates that the hydroxyl group in $Mn_xZn_{1-x}Fe_2O_4$ disappeared because of the roasting process. There was a slight blueshift about the bending vibration of the Bi–O bond (from 610 cm^{-1} to 609 cm^{-1}) and the stretching vibration of the Fe–O–Fe bond (from 1399 cm^{-1} to 1395 cm^{-1}). Moreover, the stretching vibration of Zn–O bond (569 cm^{-1}) could be seen in $Bi_5O_7I/Mn_xZn_{1-x}Fe_2O_4$.

The chemical composition and state of the $Bi_5O_7I/Mn_xZn_{1-x}Fe_2O_4$ sample were investigated using XPS. The survey spectra in Figure 3a reveal that the elements of Bi, I, O, Mn, Zn, and Fe exist in $Bi_5O_7I/Mn_xZn_{1-x}Fe_2O_4$. The atomic percentages of Bi, I, O, Mn, Zn, and Fe were 27.4%, 3.74%, 58.13%, 6.51%, 0.35%, and 3.87%, respectively. Figure 3b describes that the two characteristic peaks of

Bi $4f_{5/2}$ and Bi $4f_{7/2}$ were located at 163.8 eV and 158.5 eV in the high-resolution spectra. The I $3d_{3/2}$ and I $3d_{5/2}$ peaks in Figure 3c could be fitted with two peaks at 629.6 eV and 618.4 eV. As can be seen from Figure 3d–g, the signals at 529.2 eV, 640.6 eV, 1020.4eV, and 709.1eV were attributed to the O 1*s*, Mn 2*p*, Zn 2*p*, and Fe 2*p* orbitals, respectively.

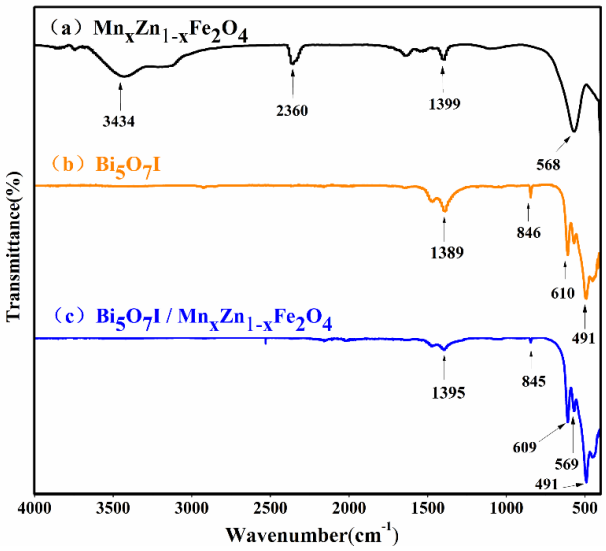

Figure 2. (**a**) Fourier-transform infrared (FTIR) spectrum of $Mn_xZn_{1-x}Fe_2O_4$; (**b**) FTIR spectrum of Bi_5O_7I; (**c**) FTIR spectrum of $Bi_5O_7I/Mn_xZn_{1-x}Fe_2O_4$.

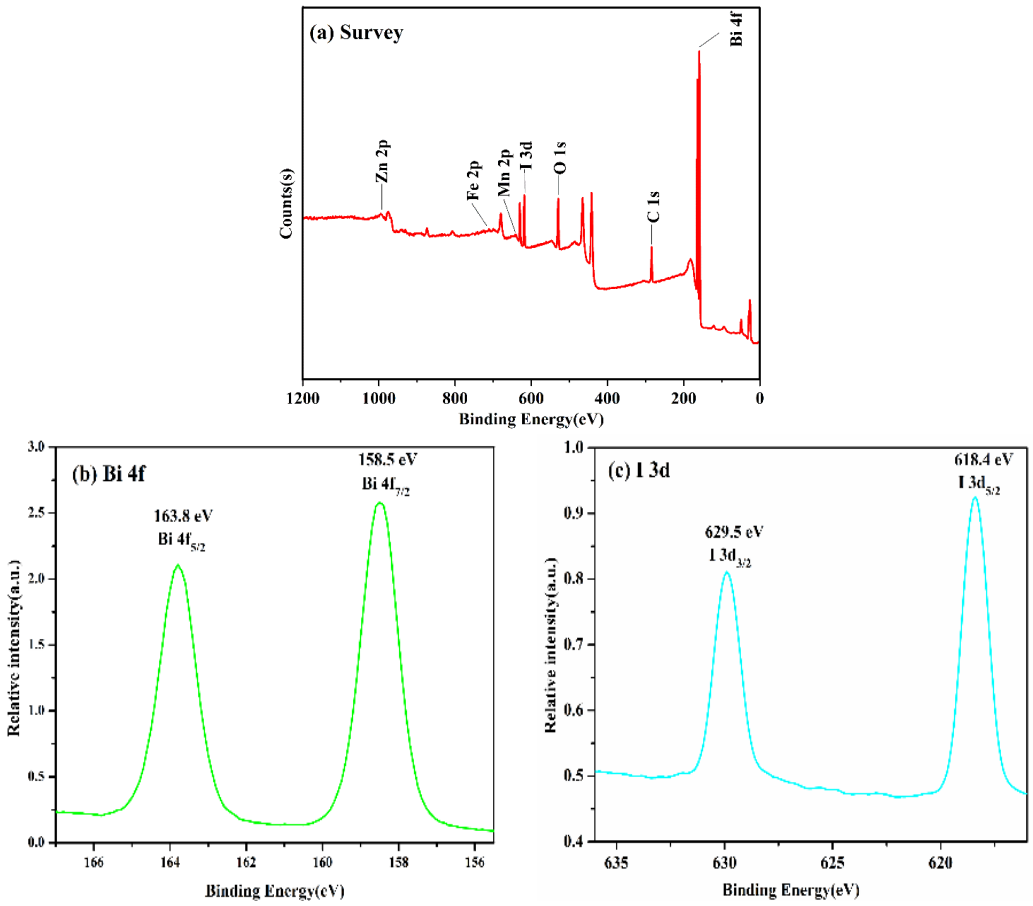

Figure 3. *Cont.*

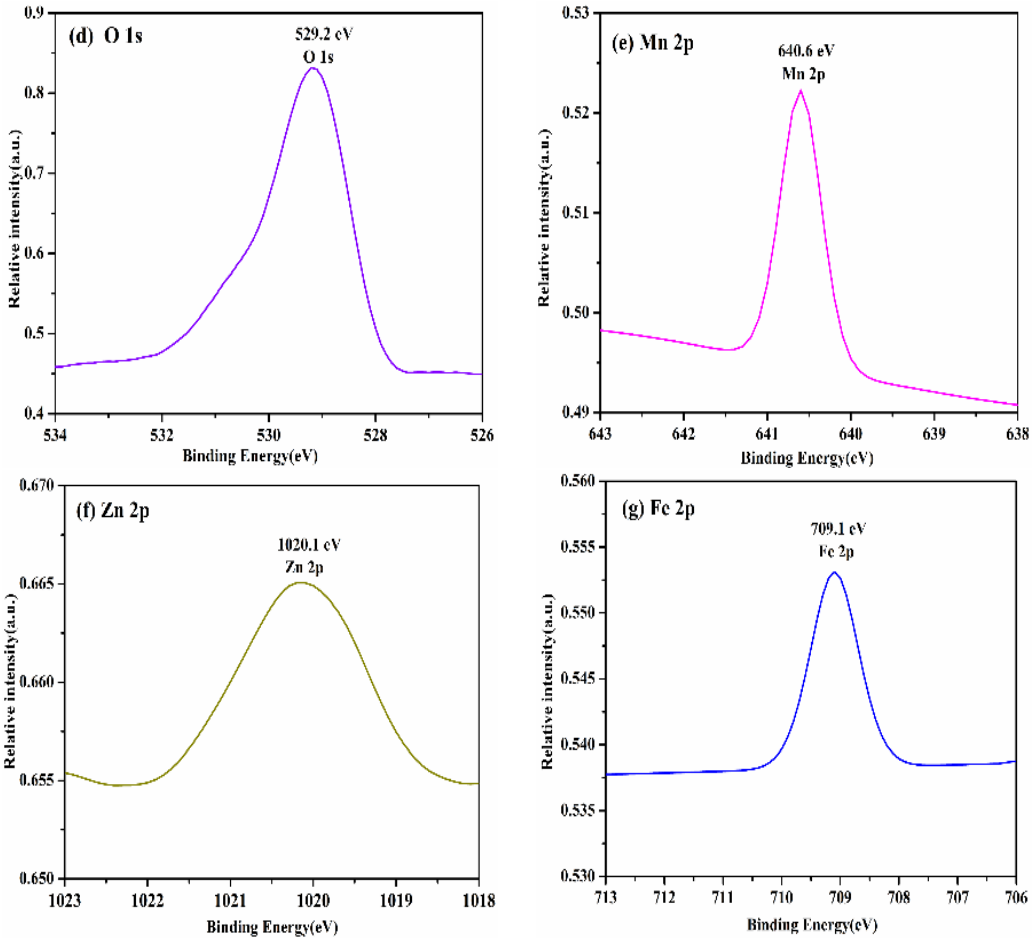

Figure 3. (**a**) X-ray photoelectron spectroscopy (XPS) survey spectra; (**b**–**g**) corresponding high-resolution XPS spectra of each element.

In order to observe the morphology of the materials, the samples were characterized by SEM. As seen from Figure 4, Bi_5O_7I was composed of irregularly shaped nanosheets, while $Mn_xZn_{1-x}Fe_2O_4$ was a spherical particle. The layer thickness of the nanosheets was around 40–60 nm, as shown in Figure 4c. The energy-dispersive X-ray spectroscopy (EDS) spectrum confirmed that the particles in Figure 4c were $Mn_xZn_{1-x}Fe_2O_4$, demonstrating the successful creation of the $Mn_xZn_{1-x}Fe_2O_4$ and Bi_5O_7I compound.

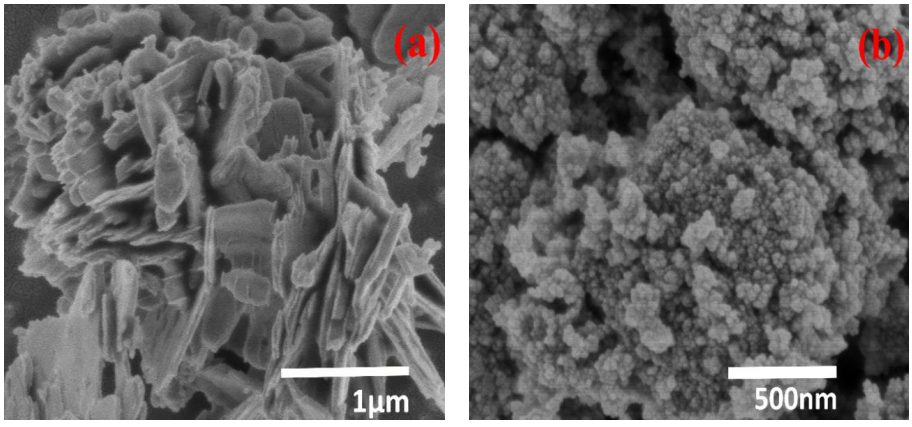

Figure 4. *Cont.*

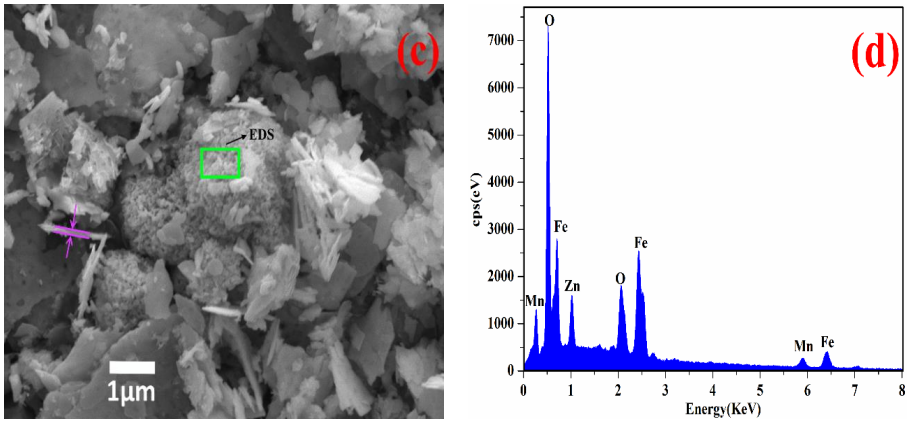

Figure 4. (**a**) SEM image of Bi_5O_7I; (**b**) SEM image of $Mn_xZn_{1-x}Fe_2O_4$; (**c**) SEM image of Bi_5O_7I/$Mn_xZn_{1-x}Fe_2O_4$; (**d**) energy-dispersive X-ray spectroscopy (EDS) spectrum of $Mn_xZn_{1-x}Fe_2O_4$.

Figure 5a,b display that lots of irregular holes on the sample surface existed. At the same time, many particles of $Mn_xZn_{1-x}Fe_2O_4$ were in contact with the gray shells of Bi_5O_7I. The high-resolution TEM (HRTEM) image of the circular region in Figure 5b reveals that $Bi_5O_7I/Mn_xZn_{1-x}Fe_2O_4$ was polycrystalline due to the different orientation of the crystal surface. The three fringe spacings of 0.321 nm, 0.277 nm, and 0.281 nm between neighboring crystal lattices corresponded to the crystal surface (312), (204), and (004) of the Bi_5O_7I crystal, and the fringe spacing of 0.251 nm corresponded to the crystal surface (311) of $Mn_xZn_{1-x}Fe_2O_4$. The EDS result proved the existence of Bi, I, O, Mn, Zn, and Fe elements, consistent with the XPS investigation.

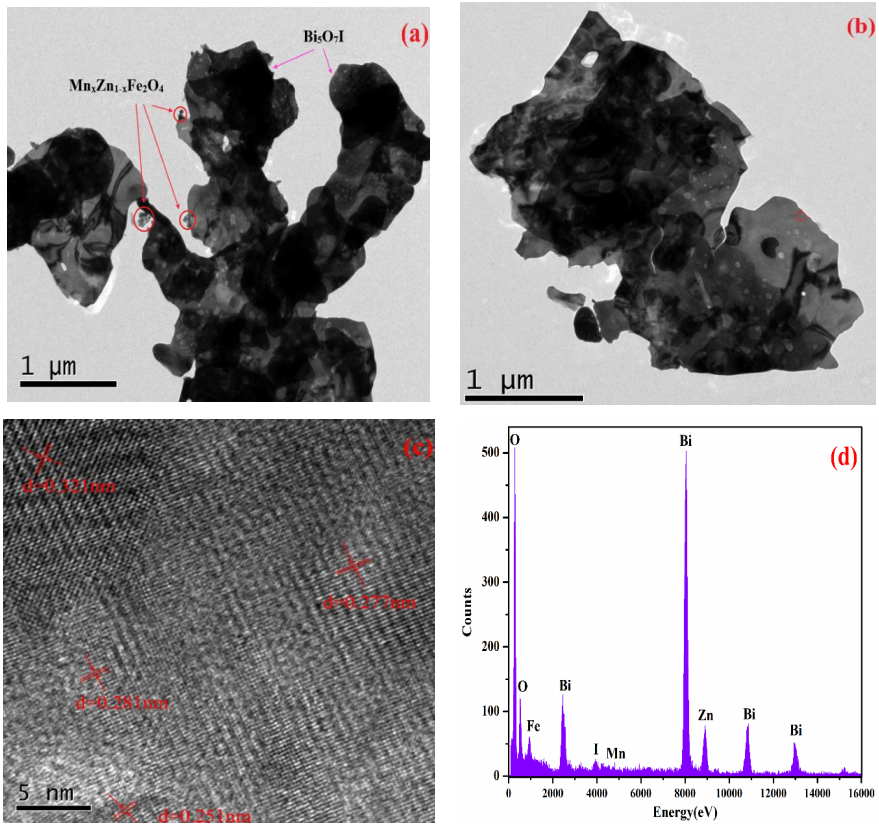

Figure 5. (**a**,**b**) TEM image of $Bi_5O_7I/Mn_xZn_{1-x}Fe_2O_4$; (**c**) high-resolution TEM (HRTEM) image of $Bi_5O_7I/Mn_xZn_{1-x}Fe_2O_4$; (**d**) EDS spectrum of $Bi_5O_7I/Mn_xZn_{1-x}Fe_2O_4$.

A specific surface analyzer was utilized to research the specific surface area and pore diameter distribution of $Bi_5O_7I/Mn_xZn_{1-x}Fe_2O_4$. From Figure 6, according to the Brunauer isotherm classification method, the adsorption–desorption isotherm belonged to class IV. The pore diameter distribution curve described that the most probable pore size of $Bi_5O_7I/Mn_xZn_{1-x}Fe_2O_4$ was 24.1 nm. Furthermore, the specific surface area of the $Bi_5O_7I/Mn_xZn_{1-x}Fe_2O_4$ sample calculated using the Brunauer–Emmett–Teller (BET) model was 7.07 m^2/g.

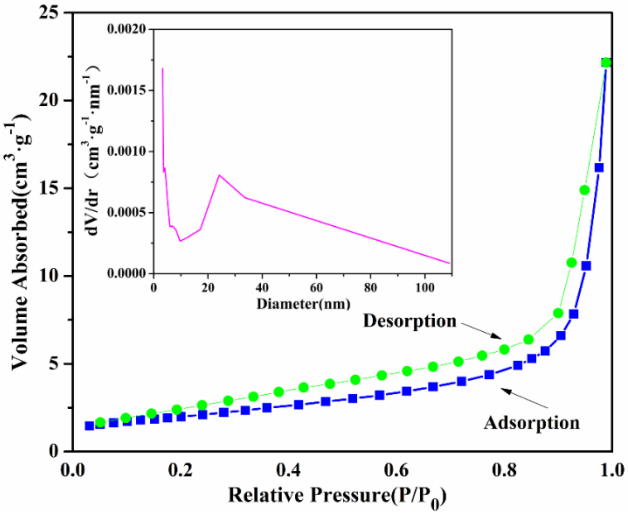

Figure 6. The N_2 adsorption–desorption isotherm of $Bi_5O_7I/Mn_xZn_{1-x}Fe_2O_4$. The pore diameter distribution curve is shown in the inset image.

3.2. Absorption Light Ability and Magnetic Properties

The UV-Vis DRS and the $(ahv)^{1/2}-hv$ curve are shown in Figure 7. The largest absorption wavelengths of Bi_5O_7I and $Bi_5O_7I/Mn_xZn_{1-x}Fe_2O_4$ were 470 nm and 600 nm, respectively, illustrating that both could absorb ultraviolet and visible light, and that adding $Mn_xZn_{1-x}Fe_2O_4$ extended the range of absorption light. Moreover, the band-gap energy of the samples could be obtained using Equation (1) [22].

$$ahv = A\left(hv - E_g\right)^{\frac{n}{2}}, \quad (1)$$

where α, h, v, and E_g are the absorption coefficient, Planck constant, light frequency, and bandgap width, respectively. A is a constant, and n depends on the transition type of the semiconductor optical carriers (direct transition, n = 1; indirect transition, n = 4). According to the plots of $(ahv)^{1/2}-hv$, the band-gap energies of Bi_5O_7I and $Bi_5O_7I/Mn_xZn_{1-x}Fe_2O_4$ were determined to be 3.27 eV and 3.22 eV, respectively.

In general, the magnetic performance of catalysts determines the recovery efficiency. Therefore, the magnetic hysteresis loops of the samples were measured. Figure 8b depicts that the saturation magnetization (Ms), coercivity (Hc), and residual magnetization (Mr) of $Bi_5O_7I/Mn_xZn_{1-x}Fe_2O_4$ were 3.9 emu/g, 126.6 Oe, and 0.7 emu/g, respectively. Compared with $Mn_xZn_{1-x}Fe_2O_4$, Ms declined because the mass ratio of magnetic materials in the photocatalyst was only 10%. It is worth noting that $Bi_5O_7I/Mn_xZn_{1-x}Fe_2O_4$ is easy to magnetize or demagnetize, and its hysteresis loss was small in the alternating magnetic field. Figure 8d shows that the particles of $Bi_5O_7I/Mn_xZn_{1-x}Fe_2O_4$ in the suspension (the right bottle) moved to the magnet rapidly when a magnet was placed close to the bottle, and the suspension became clear after 4 min. However, the suspension containing Bi_5O_7I (the left bottle) did not show any obvious change under the same conditions. From the above analysis, it was determined that the composite photocatalyst has great magnetic separation capabilities.

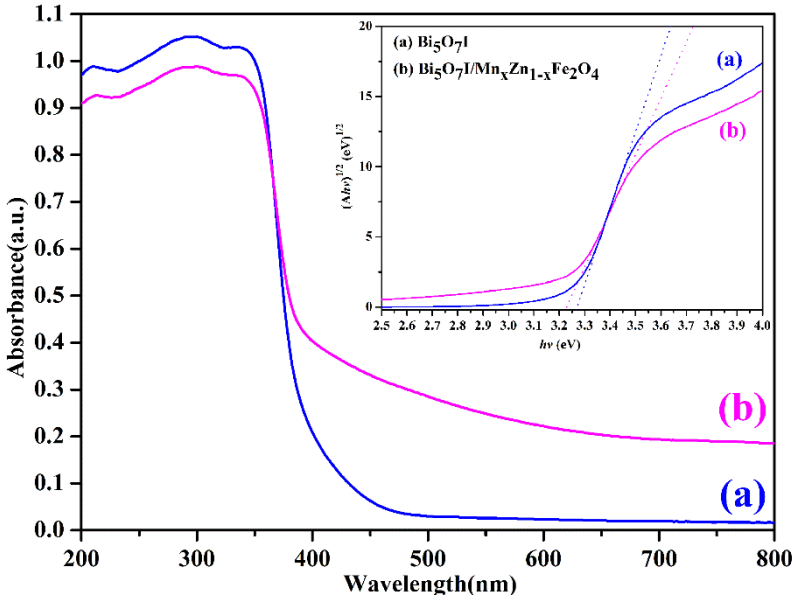

Figure 7. (**a**) Ultraviolet-visible light (UV-Vis) diffuse reflectance spectrum of Bi_5O_7I; (**b**) UV-Vis diffuse reflectance spectrum of $Bi_5O_7I/Mn_xZn_{1-x}Fe_2O_4$. The $(ahv)^{1/2}-hv$ curve is shown in the inset image.

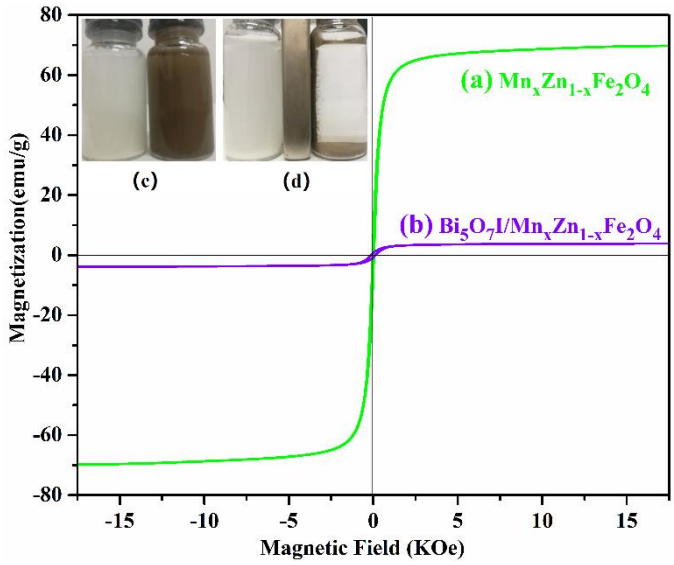

Figure 8. (**a**) The magnetic hysteresis loop of $Mn_xZn_{1-x}Fe_2O_4$; (**b**) the magnetic hysteresis loop of $Bi_5O_7I/Mn_xZn_{1-x}Fe_2O_4$. In the inset images, (**c**) the suspension of Bi_5O_7I and $Bi_5O_7I/Mn_xZn_{1-x}Fe_2O_4$, and (**d**) the suspension of Bi_5O_7I and $Bi_5O_7I/Mn_xZn_{1-x}Fe_2O_4$ are shown under the magnetic field.

3.3. Photocatalytic Activity

The photocatalytic activity of the as-prepared samples was investigated through photocatalytic degradation experiments of RhB. From Figure 9a, pure Bi_5O_7I presented the highest photocatalytic activity, whereby 97.6% of RhB was degraded within 120 min. The degradation properties of 5%, 10%, 15%, 20%, and 25% $Mn_xZn_{1-x}Fe_2O_4/Bi_5O_7I$ were 96.3%, 96.7%, 93.8%, 82.3%, and 72.7%, respectively. In addition, the first-order kinetics model given by equation $\ln(C_0/C) = kt$ was applied to quantitatively understand the reaction kinetics, where C_0 (mg·L^{-1}) is the initial concentration of RhB solution, C (mg·L^{-1}) is the concentration in aqueous solution at time t, and k (min^{-1}) is the apparent first-order kinetic constant [36]. The degradation constants (in Figure 9b) were calculated to be 0.0284, 0.0252, 0.0274, 0.0217, 0.0138, and 0.0108 min^{-1} for pure Bi_5O_7I, and 5%, 10%, 15%, 20%, and 25% $Mn_xZn_{1-x}Fe_2O_4/Bi_5O_7I$ samples, respectively. Compared with Bi_5O_7I, the photocatalytic

activity of the compounds declined for two reasons. On one hand, $Mn_xZn_{1-x}Fe_2O_4$ became the recombination center of the photogenerated electron (e^-) and hole (h^+), which reduced the lifetime of the photogenerated carriers. On the other hand, adding $Mn_xZn_{1-x}Fe_2O_4$ decreased the amount of catalyst in the compound.

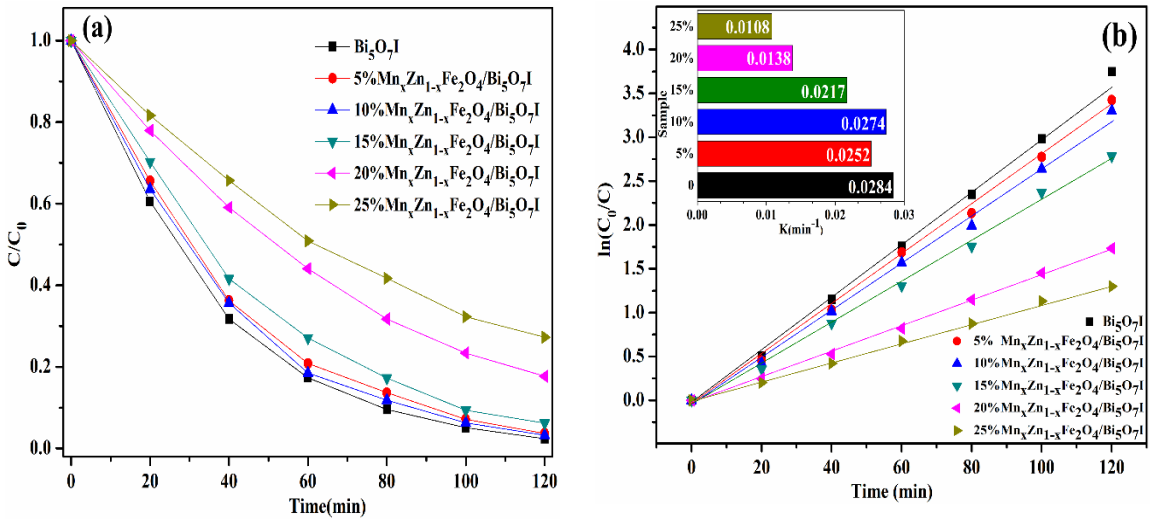

Figure 9. (**a**) Photocatalytic degradation and (**b**) kinetic linear simulation curves of Rhodamine B (RhB) over Bi_5O_7I and $Bi_5O_7I/Mn_xZn_{1-x}Fe_2O_4$.

3.4. Stability and Recycling Ability

The stability and the recycling ability of $Bi_5O_7I/Mn_xZn_{1-x}Fe_2O_4$ were studied through recycling experiments. After each reaction, the photocatalyst was separated by an external magnet and then washed with deionized water before being dried at 80 °C for 3 h. The recycling experiments show that the average recovery rate was 90.1%. Figure 10 shows that the degradation rate was still more than 81.1% after five reuses. The experimental results indicate that the composite magnetic photocatalyst can be reused several times with excellent stability.

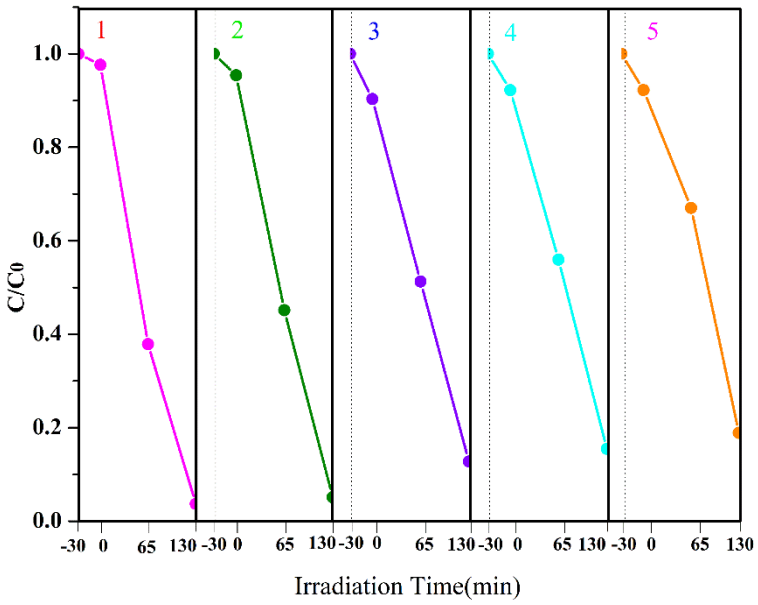

Figure 10. Degradation rate of RhB on $Bi_5O_7I/Mn_xZn_{1-x}Fe_2O_4$ after being recycled.

3.5. Photocatalytic Mechanism

There are a few reasons why the composite magnetic photocatalyst has good photocatalytic activity. Firstly, the existence of a porous structure is helpful for improving the transfer efficiency of the photogenerated electron and hole. In this structure, the distance from where photogenerated charge is generated to the semiconductor surface is shortened, which can effectively reduce the recombination of the photogenerated electron and hole [37].

Secondly, the band structure of the photocatalyst is beneficial for producing a hydroxyl radical (•OH). Figure 11 illustrates the proposed mechanism for the photocatalytic activity of $Bi_5O_7I/Mn_xZn_{1-x}Fe_2O_4$ with RhB. As is known, •OH is the major active substance in the photocatalytic degradation of organic pollutants [38]. The adsorbed water is oxidized to •OH by a hole when the valence band top has more positive redox potential than that of $•OH/H_2O$ (+2.27 eV). The position of the conduction band bottom (E_{CB}) can be obtained using Equation (2) [39].

$$E_{CB} = X - E^C - 0.5E_g, \quad (2)$$

where X is the absolute electronegativity of the semiconductor oxide, E^C is the potential energy of the free electron in a standard hydrogen electrode (~4.5 eV), and E_g is the band gap of the semiconductor oxide. The position of the conduction band bottom for the photocatalyst was determined to be 0.04 eV. Therefore, the position of the valence band top was 3.31 eV, which is sufficient to turn OH^- into •OH through oxidation.

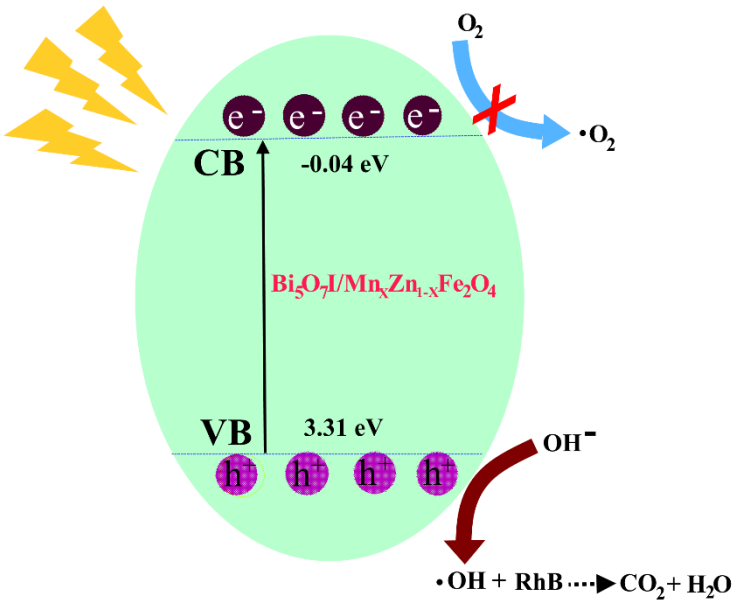

Figure 11. Schematic of the possible reaction mechanism of the photocatalytic procedure.

4. Conclusions

The composite magnetic photocatalyst $Bi_5O_7I/Mn_xZn_{1-x}Fe_2O_4$ was prepared using a hydrothermal-roasting method. This is convenient for mass production in the future because of its simple process and low cost. According to the analysis results of XRD, FTIR, XPS, SEM, and TEM, Bi_5O_7I and $Mn_xZn_{1-x}Fe_2O_4$ were successfully combined. $Bi_5O_7I/Mn_xZn_{1-x}Fe_2O_4$ is a mesoporous material, able to absorb ultraviolet and visible light. Meanwhile, $Bi_5O_7I/Mn_xZn_{1-x}Fe_2O_4$ is a soft magnetic material with great magnetic induction intensity. The photocatalytic degradation and recycling experiments revealed that $Bi_5O_7I/Mn_xZn_{1-x}Fe_2O_4$ has good photocatalytic activity and stability.

Author Contributions: Conceptualization, H.W. and L.X.; Data Curation, H.W.; Formal Analysis, Y.L. and Q.F.; Investigation, T.W. and R.W.; Methodology, H.W.; Resources, L.X.; Supervision, C.L.; Writing—Original Draft, H.W.; Writing—Review and Editing, H.W. and L.X.

Funding: This research was funded by the Chongqing Basic Science and Advanced Technology Research Program (CSTC2015jcyjBX0015) and the Natural Science Foundation of China (51374259).

Acknowledgments: The authors thank Yahan Yang and Xiang Wu for their contributions to data processing.

Conflicts of Interest: The authors declare no conflicts of interest.

References

1. Kumar, A.; Sharma, S.K.; Sharma, G. Wide spectral degradation of Norfloxacin by Ag@$BiPO_4$/BiOBr/$BiFeO_3$ nano-assembly: Elucidating the photocatalytic mechanism under different light sources. *J. Hazard. Mater.* **2019**, *364*, 429–440. [CrossRef] [PubMed]
2. Guo, F.; Shi, W.L.; Li, M.Y.; Wen, H. 2D/2D Z-scheme heterojunction of $CuInS_2$/g-C_3N_4 for enhanced visible-light-driven photocatalytic activity towards the degradation of tetracycline. *Sep. Purific. Technol.* **2019**, *210*, 608–615. [CrossRef]
3. Li, S.J.; Mo, L.Y.; Liu, Y.P.; Zhang, H.; Ge, Y.; Zhou, Y. Ag_2CO_3 Decorating BiOCOOH Microspheres with Enhanced Full-Spectrum Photocatalytic Activity for the Degradation of Toxic Pollutants. *Nanomaterials.* **2018**, *8*, 914. [CrossRef] [PubMed]
4. Mishra, Y.K.; Adelung, R. ZnO tetrapod materials for functional applications. *Mater. Today* **2018**, *21*, 631–651. [CrossRef]
5. Sharma, M.; Joshi, M.; Nigam, S.; Shree, S.; Avasthi, D.K.; Adelung, R.; Srivastava, S.K.; Mishra, Y.K. ZnO tetrapods and activated carbon based hybrid composite: Adsorbents for enhanced decontamination of hexavalent chromium from aqueous solution. *Chem. Eng. J.* **2019**, *358*, 540–551. [CrossRef]
6. Grottrup, J.; Schutt, F.; Smazna, D.; Lupan, O.; Adelung, R.; Mishra, Y.K. Porous ceramics based on hybrid inorganic tetrapodal networks for efficient photocatalysis and water purification. *Ceram. Int.* **2017**, *43*, 14915–14922. [CrossRef]
7. Huang, D.; Long, Y.J.; Luo, L.J.; Li, L.; Zhang, S.; Wang, L.; Jiang, F. Synthesis of N-doped Bi_2O_3 and its excellent visible light photocatalytic performance for the degradation of 17 beta-estradiol. *Sci. Adv. Mater.* **2019**, *11*, 105–111. [CrossRef]
8. Oppong, S.O.B.; Opoku, F.; Govender, P.P. Tuning the electronic and structural properties of Gd-TiO_2-GO nanocomposites for enhancing photodegradation of IC dye: The role of Gd^{3+} ion. *Appl. Catal. B Environ.* **2019**, *243*, 106–120. [CrossRef]
9. Han, G.; Li, D.Y.; Zheng, Y.F. Enhanced visible-light-responsive photocatalytic properties of Bi_2MoO_6-B_iOCl nanoplate composites. *J. Nanosci. Nanotechnol.* **2018**, *18*, 5575–5581. [CrossRef]
10. Wang, Y.; Tan, G.; Ren, H. Synthesis of $BiVO_4$ with surface heterojunction for enhancing photocatalytic activity by low temperature aqueous method. *Mater. Lett.* **2018**, *229*, 308–311. [CrossRef]
11. Wang, A.J.; Zhang, J.; Zhao, W.; Zhu, W.; Zhong, Q. Porphyrin decorated $Bi_2O_2CO_3$ nanocomposites with efficient difunctional properties of photocatalysis and optical nonlinearity. *J. Alloy. Compd.* **2018**, *748*, 929–937. [CrossRef]
12. Wu, Y.; Li, M.; Yuan, J. A facile pechini method to synthesize novel $Bi_{12}SiO_{20}$-Bi_2SiO_5 heterostructure photocatalysts with enhanced visible light photocatalytic activity. *J. Mater. Sci. Mater. Electron.* **2018**, *29*, 4503–4508. [CrossRef]
13. Ketterer, J.; Keller, E.; Kramer, V. Crystal-structure of bismuth oxide iodide, beta-Bi_5O_7I. *Z. Kristallorgr.* **1985**, *172*, 63–70. [CrossRef]
14. Peng, Y.; Mao, Y.G.; Liu, T. Synthesis of one-dimensional Bi_2O_3-Bi_5O_7I heterojunctions with high interface quality. *Crystengcomm.* **2018**, *20*, 4771–4780. [CrossRef]
15. Liang, C.; Niu, C.G.; Zhang, L.; Wen, X.J.; Yang, S.F.; Guo, H.; Zeng, G.M. Construction of 2D heterojunction system with enhanced photocatalytic performance: Plasmonic Bi and reduced graphene oxide co-modified Bi_5O_7I with high-speed charge transfer channels. *J. Hazard. Mater.* **2019**, *361*, 245–258. [CrossRef] [PubMed]
16. Huang, W.L. Electronic structures and optical properties of BiOX (X = F, Cl, Br, I) via DFT Calculations. *J. Comput. Chem.* **2009**, *30*, 1882–1891. [CrossRef] [PubMed]

17. Sangita, D.; Tilak, D.; Soumendu, D. Impact of bi-axial strain on the structural, electronic and optical properties of photo-catalytic bulk bismuth oxyhalides. *Phys. Chem. Chem. Phys.* **2017**, *20*, 103–111.
18. Yang, N.; Lv, X.; Zhong, S.T.; Qian, D.; Han, S.; Li, D.; Geng, X.; Fang, H.; Jiang, W. Preparation of Z-scheme AgI/Bi_5O_7I plate with high visible light photocatalytic performance by phase transition and morphological transformation of BiOI microspheres at room temperature. *Dalton Trans.* **2018**, *47*, 11420–11428. [CrossRef]
19. Fu, H.; Pan, C.; Yao, W.; Zhu, Y. Visible-light-induced degradation of rhodamine B by nanosized Bi_2WO_6. *J. Phys. Chem. B* **2005**, *109*, 22432–22439. [CrossRef]
20. Fu, J.-Y.; Chen, L.-W.; Dai, Y.-M.; Liu, F.-Y.; Huang, S.-T.; Chen, C.-C. BiO_mF_n/BiO_xI_y/GO Nanocomposites: Synthesis, characterization, and photocatalytic activity. *Mol. Catal.* **2018**, *455*, 214–223. [CrossRef]
21. Kudo, A.; Omori, K.; Kato, H. A novel aqueous process for preparation of crystal form-controlled and highly crystalline $BiVO_4$ powder from layered vanadates at room temperature and its photocatalytic and photophysical properties. *J. Am. Chem. Soc.* **1999**, *121*, 11459–11467. [CrossRef]
22. Sun, S.M.; Wang, W.Z.; Zhang, L.; Zhou, L.; Yin, W.; Shang, M. Visible light-induced efficient contaminant removal by Bi_5O_7I. *Environ. Sci. Technol.* **2009**, *43*, 2005–2010. [CrossRef] [PubMed]
23. Xia, Y.; He, Z.; Su, J.; Tang, B.; Liu, Y. Enhanced photocatalytic performance of Z-scheme Cu_2O/Bi_5O_7I nanocomposites. *J. Mater. Sci. Mater. Electron.* **2018**, *29*, 15271–15281. [CrossRef]
24. Wang, C.; Zhu, L.; Chang, C.; Fu, Y.; Chu, X. Preparation of magnetic composite photocatalyst $Bi_2WO_6/CoFe_2O_4$ by two-step hydrothermal method and itsphotocatalytic degradation of bisphenol A. *Catal. Commun.* **2013**, *37*, 92–95. [CrossRef]
25. Liu, Y.B.; Zhu, G.Q.; Gao, J.Z.; Zhu, R.; Hojamberdiev, M.; Wang, C.; Wei, X.; Liu, P. A novel synergy of Er^{3+}/Fe^{3+} co-doped porous Bi_5O_7I microspheres with enhanced photocatalytic activity under visible-light irradiation. *Appl. Catal. B Environ.* **2017**, *205*, 421–432. [CrossRef]
26. Chen, X.J.; Dai, Y.Z.; Wang, X.Y.; Guo, J.; Liu, T.H.; Li, F.F. Synthesis and characterization of Ag_3PO_4 immobilized with graphene oxide (GO) for enhanced photocatalytic activity and stability over 2,4-dichlorophenol under visible light irradiation. *J. Hazard. Mater.* **2015**, *292*, 9–18. [CrossRef]
27. Wang, S.; Chen, Y.; Long, Y.J.; Li, L.; Wang, L.; Zhang, S.; Jiang, F. Room Temperature Synthesis of BiOI/Bi_5O_7I p-n Heterojunction with Enhanced Photocatalytic Activity for 17 alpha-Ethynylestradiol. *ChemistrySelect* **2018**, *3*, 8095–8105. [CrossRef]
28. Zhang, Y.F.; Zhu, G.Q.; Gao, J.Z; Zhu, R.; Hojamberdiev, M.; Wang, C.; Liu, P. Superior-performance spherical-like Eu-doped Bi_5O_7I photocatalysts for the removal of organic pollutants under visible-light irradiation. *J. Mater. Sci. Mater. Electron.* **2017**, *28*, 11034–11045. [CrossRef]
29. Geng, X.Q.; Chen, S.; Lv, X.; Jiang, W.; Wang, T. Synthesis of g-C_3N_4/Bi_5O_7I microspheres with enhanced photocatalytic activity under visible light. *Appl. Surf. Sci.* **2018**, *462*, 18–28. [CrossRef]
30. Kermani, M.; Kakavandi, B.; Farzadkia, M. Catalytic ozonation of high concentrations of catechol over TiO_2@Fe_3O_4 magnetic core-shell nanocatalyst: Optimization, toxicity and degradation pathway studies. *J. Clean. Prod.* **2018**, *192*, 597–607. [CrossRef]
31. Gimenes, R.; Baldissera, M.R.; da Silva, M.R.A.; da Silveira, C.A.; Soares, D.A.W.; Perazolli, L.A.; da Silva, M.R.; Zaghete, M.A. Structural and magnetic characterization of $Mn_xZn_{1-x}Fe_2O_4$ (x = 0.2; 0.35; 0.65; 0.8; 1.0) ferrites obtained by the citrate precursor method. *Ceram. Int.* **2012**, *38*, 741–746. [CrossRef]
32. Zhang, Z.D.; Xu, L.J.; Liu, C.L. Preparation and characterization of composite magnetic photocatalyst $Mn_xZn_{1-x}Fe_2O_4$/beta-Bi_2O_3. *RSC Adv.* **2015**, *5*, 79997–80004. [CrossRef]
33. Liu, Z.; Xu, W.; Fang, J. Decoration of BiOI quantum size nanoparticles with reduced graphene oxide in enhanced visible-light-driven photocatalytic studies. *Appl. Surf. Sci.* **2012**, *259*, 441–447. [CrossRef]
34. Xie, T.P.; Li, H.; Liu, C.L.; Yang, J.; Xiao, T.; Xu, L. Magnetic Photocatalyst $BiVO_4$/Mn-Zn ferrite/Reduced Graphene Oxide: Synthesis Strategy and Its Highly Photocatalytic Activity. *Nanomaterials* **2018**, *8*, 380. [CrossRef] [PubMed]
35. Sun, Y.Y.; Wu, J.; Ma, T.J.; Wang, P.; Cui, C.; Ma, D. Synthesis of C@Bi_2MoO_6 nanocomposites with enhanced visible light photocatalytic activity. *Appl. Surf. Sci.* **2017**, *403*, 141–150. [CrossRef]
36. Chang, M.J.; Cui, W.N.; Wang, H.; Liu, J.; Li, H.L.; Du, H.L.; Peng, L.G. Recoverable magnetic $CoFe_2O_4$/BiOI nanofibers for efficient visible light photocatalysis. *Colloid Surf. A* **2019**, *562*, 127–135. [CrossRef]
37. Yang, J.; Xu, L. J.; Liu, C.L.; Xie, T. Preparation and photocatalytic activity of porous Bi_5O_7I nanosheets. *Appl. Surf. Sci.* **2014**, *319*, 265–271. [CrossRef]

38. Chen, L.; Huang, R. Room-temperature synthesis of flower-like BiOX (X = Cl, Br, I) hierarchical structures and their visible-light photocatalytic activity. *Inorg. Chem.* **2013**, *52*, 11118–11125. [CrossRef]
39. Babu, V.J.; Bhavatharinib, R.S.R. Electrospun BiOI nano/microtectonic plate-like structure synthesis and UV-light assisted photodegradation of ARS dye. *RSC Adv.* **2014**, *4*, 19251–19256. [CrossRef]